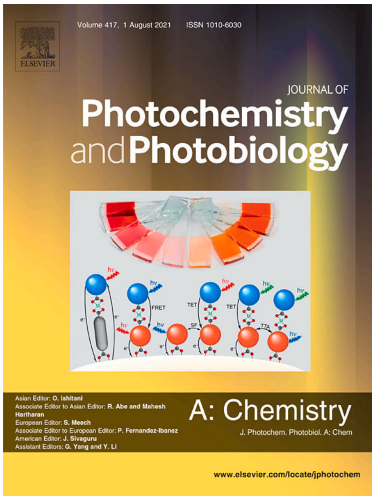

Invited paper

Kinetic study of *p*-nitrophenol degradation with zinc oxide nanoparticles prepared by sol–gel methods

Antoine Farcy, Julien G. Mahy, Christelle Alié, Joachim Caucheteux, Dirk Poelman, Zetian Yang, Pierre Eloy, Nathalie Body, Sophie Hermans, Benoît Heinrichs, Stéphanie D. Lambert

PII:	S1010-6030(24)00348-4
DOI:	https://doi.org/10.1016/j.jphotochem.2024.115804
Reference:	JPC 115804

To appear in:	*Journal of Photochemistry & Photobiology, A: Chemistry*

Received Date:	12 December 2023
Revised Date:	14 May 2024
Accepted Date:	31 May 2024

Please cite this article as: A. Farcy, J.G. Mahy, C. Alié, J. Caucheteux, D. Poelman, Z. Yang, P. Eloy, N. Body, S. Hermans, B. Heinrichs, S.D. Lambert, Kinetic study of *p*-nitrophenol degradation with zinc oxide nanoparticles prepared by sol–gel methods, *Journal of Photochemistry & Photobiology, A: Chemistry* (2024), doi: https://doi.org/10.1016/j.jphotochem.2024.115804

Kinetic study of *p*-nitrophenol degradation with zinc oxide nanoparticles prepared by sol-gel methods

Antoine Farcy [1*], Julien G. Mahy [1,4]*, Christelle Alié [1], Joachim Caucheteux [1], Dirk Poelman [2], Zetian Yang [2], Pierre Eloy [3], Nathalie Body [3], Sophie Hermans [3], Benoît Heinrichs [1], Stéphanie D. Lambert [1]

[1] Department of Chemical Engineering – Nanomaterials, Catalysis, & Electrochemistry, University of Liège, B6a, Quartier Agora, Allée du Six Août 11, 4000 Liège, Belgium

[2] LumiLab, Department of Solid State Sciences, Ghent University, Krijgslaan 281-S1, Ghent B-9000, Belgium

[3] Institute of Condensed Matter and Nanosciences – Molecular Chemistry, Materials and Catalysis (IMCN/MOST), Université Catholique de Louvain, Place Louis Pasteur 1, Box L4.01.03, 1348 Louvain-La-Neuve, Belgium

[4] Institut National de la Recherche Scientifique (INRS), Centre Eau Terre Environnement, Université du Québec, 490, Rue de la Couronne, Québec (QC), G1K 9A9, Canada

*Corresponding authors: Antoine Farcy, email: antoine.farcy@uliege.be; Julien G. Mahy, email: julien.mahy@uliege.be; address: Allée du Six Août 11, 4000 Liège, Belgium

Abstract

Three zinc oxides (ZnO A, B, C) with similar spherical morphology but different sizes are synthesized by sol-gel methods. A kinetic study is carried out on the photocatalytic activity of these three ZnO, through the degradation of *p*-nitrophenol (PNP). A mathematical model is developed and the rate constants of the three catalysts are determined. To understand the parameters influencing the kinetics, the catalysts are reduced to the surface of an isolated particle (assuming perfect dispersion conditions where all catalytic active sites are available) whose size is determined by X-ray diffraction (XRD) and transmission electron microscopy (TEM). However, by considering the real case (not a perfect dispersion), it appears that the size of the aggregates induced by the synthesis methods play a more important role in the catalytic activity of the three ZnO samples than defects. A discussion on the formation of these aggregates highlights the importance of the synthesis parameters, like the solvent or the surfactant used to obtain a high dispersion. The dispersion plays a crucial role in photocatalytic efficiency, with kinetics three times higher for the catalyst with the best dispersion. Also, as shown by photoluminescence and X-ray photoelectron spectroscopy (XPS), the type and amount of defects play an important role in the photocatalytic performance. ZnO A and B show a defect peak at 620 nm whereas ZnO C shows a defect peak at 680 nm, suggesting a different type of defect on the surface of the catalyst that reduces the photocatalytic performance. Electron paramagnetic resonance (EPR) measurements are performed to identify the type of radicals involved in PNP degradation. The results show that the catalyst with the best dispersion produces the highest amount of hydroxyl radicals. Finally, photoluminescence and XPS analyses underline the type and the amount of defects for the three photocatalysts.

Keywords: structure defects, catalyst dispersion, photocatalysis, water treatment, kinetics, ZnO

1. Introduction

Water is the basis of life, it is essential but this resource is not inexhaustible, so it is necessary to be able to preserve and recycle it. The growing industrial activities of mankind, in order to meet market demand, are constantly increasing the amount of waste discharged, particularly into water, polluting it and rendering it unsuitable for consumption [1]. For decades, scientists have been working to minimize the impact of this industrial development on water quality. Several techniques have been developed to purify water, including filtration and/or biological treatment in wastewater treatment plants to reduce the pollutants present in the water [2]. However, these techniques have their shortcomings when attempting to degrade organic molecules present in trace amounts [3].

Advanced oxidation processes (AOPs) have been developed to solve this type of problem [4]. This involves producing powerful chemical species in the aqueous phase, known as radicals, which can degrade a wider range of molecules compared to traditional methods [5]. Among these methods, heterogeneous photocatalysis offers several advantages, including simple synthesis of semiconductors used as catalysts, environmental friendliness, and low energy consumption [6].

One photocatalyst attracting particular attention is zinc oxide, because it is non-toxic unlike similar types of catalysts (for example titanium dioxide), has a bandgap of 3.3 eV and is easy to synthesize, inexpensive, and environmentally friendly. There are various methods for synthesizing zinc oxide, including two main routes: physical and chemical. Chemical routes include solvothermal [7], hydrothermal [8], microwave [9], and sol-gel methods [10], for example. The sol-gel method has the advantage of being easy to implement with low environmental impact and low energy cost and will be used in this paper [11]. Moreover, the use of sol-gel methods makes it possible to address a number of issues concerning ZnO synthesis, which this article sets out to resolve, *i.e.*, lowering the synthesis temperature of the materials, controlling their morphology and size and, consequently, their specific surface area, which are key parameters in the design of photocatalysts [12].

In this study, ZnO catalysts are synthesized in three different ways. The morphology is studied by scanning electron microscopy (SEM) and transmission electron microscopy (TEM). Also, the presence of defects is investigated by photoluminescence (PL) and X-ray photoelectron spectroscopy (XPS). In addition, dispersion in solution is measured by dynamic light scattering (DLS), zeta potential measurements, and TEM. The photodegradation efficiency is evaluated on a model pollutant, *p*-nitrophenol (PNP). A kinetic study of the PNP degradation is made with and without scavenger to build a model fitting the experimental data. Also, electron paramagnetic resonance (EPR) experiments using a spin trap reinforce the results obtained from the scavenger study, shedding light on the kinetics of hydroxyl radical production by the different catalysts. This kinetic study aims to highlight the physico-chemical parameters that have the greatest influence on the degradation of PNP in order to design efficient ZnO catalysts.

2. Materials and methods

2.1 Synthesis of photocatalysts

2.1.1 ZnO A

5.9 g of zinc acetate dihydrate ($Zn(CH_3COO)_2.2H_2O$, VWR CHEMICALS, Netherlands) are dissolved in 250 mL of ethanol at 80°C under stirring. After dissolution, the temperature is decreased to 60°C. At the same time, 4.5 g of KOH are dissolved in 130 mL of ethanol at room temperature and this solution is heated to 60°C. The KOH is then added dropwise into the zinc acetate solution at 60°C and the solution is kept under agitation at 60°C for 6 h. After the reaction, the solid from the suspension is washed three times with ethanol (C_2H_6O, MERCK, Germany) and dried in an oven for 12 h at 100°C.

2.1.2 ZnO B

Zinc acetate dihydrate (16.2 g) is dissolved in 250 mL of diethyleneglycol (DEG) ($C_4H_{10}O_3$, MERCK, Germany) and the temperature is increased to 140°C to achieve complete dissolution. Then, the temperature is increased to 180°C and the solution becomes opaque and white. The mixture is left under stirring for 2 h. After that time, the suspension is centrifuged and the solid is washed three times with ethanol. The resulting powder is dried at 100°C for 12 h.

2.1.3 ZnO C

Zinc acetate dihydrate is dissolved in ethanol with the assistance of ethanolamine (EA) ($NH_2C_2H_4OH$, SIGMA-ALDRICH, Germany) at room temperature. In a typical synthesis, 10.98 g of ZnAc and 3.05 g of EA are mixed in 160 g of ethanol. The precursor solution is stirred for 10 min. Since the zinc oxide is not directly formed in the solution, a thermal treatment is required, which is done at 550°C for 2 h, under static air, resulting in a grey powder.

2.2 Sample characterization

Crystallite structure and phases are determined using a Bruker D8 Twin-Twin X-Ray diffractometer with Cu-Kα radiation of 1.54 Å in a range between 2 θ = 10° to 70°. Crystallite size of the different samples is estimated using the Scherrer formula:

$$d = \frac{K\lambda}{\beta \cos(\theta)} \quad (1)$$

where K is a shape factor (0.9), λ is the X-ray wavelength (1.54 Å), β is the full width half maximum, and θ is the Bragg angle.

XPS analyses are done using an SSI-X-probe 100/206 spectrometer (Surface Science Instruments), equipped with a flood gun (8 eV) for surface charge neutralization. Samples on an adhesive support are introduced into a Macor® carousel topped with a nickel grid in order to avoid charge effects. Analyses are done at room temperature with an analysis chamber pressure of 10^{-6} Pa. The main peaks analyzed for the three samples are C 1s, O 1s, and Zn 2p. Data treatment is executed with the CasaXPS software (Casa Software Ltd., Teignmouth, UK) using a Gaussian/Lorentzian (85/15) decomposition treatment and a Shirley-type baseline subtraction. All XPS spectra are calibrated using the C–(C,H) component of the C 1s peak localized at 284.8 eV.

Nitrogen adsorption-desorption isotherms are collected on a micromeritics ASAP 2420 at a temperature of −196°C. Before measurements, samples are degassed under high vacuum at 80°C for 15 h. The specific surface area (S_{BET}) is determined using the Brunauer Emmett and Teller (BET) equation by taking the relative pressure data between 0.05 and 0.25.

Morphologies of the three powders are obtained by scanning electron microscopy (SEM) on a TESCAN CLARA device from Bruker operating at 15 keV. The samples, previously dispersed in acetone in an ultrasonic bath for 2 min, are placed on a glass slide. The surface is coated with gold before being introduced under the microscope.

Transmission electron microscopy (TEM) is done by taking 30 µL of the samples, previously diluted in water and sonicated for 30 min, placed on 200 mesh Formvar/carbon nickel grids (Laborimpex, Brussels, Belgium). Samples are dried, examined with a TEM (Jeol JEM1400, Jeol, Zaventem, Belgium) at 80 kV and photographed with an 11-megapixel bottom-mounted TEM camera system (Quemesa, Olympus).

The diffuse reflectance (DRS) measurements are performed using a PerkinElmer Lambda1050 UV-vis-NIR spectrophotometer equipped with a Spectralon-coated integrating sphere with PMT (photomultiplier) and InGaAs detectors. The spectra are transformed using the Kubelka–Munk function to produce a signal, normalized for comparison between samples, enabling the band gaps to be calculated. The details of this treatment method are widely described elsewhere [13].

Photoluminescence emission (PL) and excitation (PLE) spectra are recorded using an Edinburgh FS920 (Edinburgh Instruments Ltd, Livingston, UK) fluorescence spectrometer, using a 450 W xenon arc lamp as excitation source. Samples are fixed on a metallic plate using double-sided non-luminescent tape. The wavelength of the incident light is the same for the three samples to be analyzed, *i.e.*, 325 nm. PL spectra are monitored over a range of 350 to 800 nm in a step of 0.5 nm, which allows the entire zinc oxide gap to be scanned. The experiments are performed at room temperature. To overcome the problems associated with measuring sample mass, area-under-curve ratios of the photoluminescence spectra are used to compare the three catalysts in terms of number of defects.

The zeta potential and hydrodynamic diameter are measured on the different sols with a DelsaNano C device from Beckman Coulter, giving information about colloid stability. All the samples are sonicated beforehand for 10 min to reach the highest dispersion.

Electron paramagnetic resonance (EPR) experiments are done at room temperature using a Bruker EMX micro and 5,5-dimethyl-1-pyrroline N-oxide (DMPO) as a spin trap. The modulation frequency is set to 100 kHz and the amplitude modulation is set to 1 Gauss. Resolution is set to 1024 and 4 spectra are acquired for each sample. In a typical experiment, 10 mg of catalyst are dispersed in 10 mL of Milli-Q water. 100 µL of DMPO are added to the suspension and it is irradiated under UV-A for 150 s to produce radicals. A capillary tube is used to put the solution in the EPR cavity.

2.3 Photocatalytic experiment

Photocatalytic performances of the different synthesized powders are evaluated by the degradation of a model pollutant, *p*-nitrophenol (PNP).

For this purpose, cellular wells are filled with 10 mg of the zinc oxide, previously ground in a mortar, and dispersed in 10 mL of a 10^{-4} M PNP aqueous solution. They are placed in a box under a UV-A lamp (wavelength λ = 365 nm and intensity of 1.2 mW/cm^2; model: Osram Sylvania, Blacklight-Blue Lamp, F18W/BLB-T8) with a fan system to maintain a constant temperature of 20°C.

In parallel, to distinguish photocatalytic degradation of PNP from adsorption, duplicates of all samples are made and placed in the dark.

2.3.1 Kinetic model

1.5 mL of solution is taken at regular intervals to monitor the degradation of the PNP over time. Four points are considered to establish the pollutant degradation constant reaction rate, k.

Considering a homogeneous dispersion of the powder in the PNP solution, the kinetic parameters of the three catalysts are found by determining mass balance of the pollutant as described by Heinrichs et al. [14]. Briefly:

$$\frac{dn}{dt} = -rm - V_s C \ (2)$$

With $V = V_0 - V_s t$

Where n is the mole number of the pollutant, r is the specific reaction rate, m is the mass of the catalyst, V_s is the flow rate of the pollutant, V_0 is the initial solution volume, V the solution volume, C is the concentration of the pollutant and t is the time. It is assumed that the reaction is first order, so $r = kC$.

As cellular wells are filled with PNP and catalyst, there is no flow rate and equation (2) becomes:

$$\frac{dC}{dt} = -kC\frac{m}{V_0} \ (3)$$

By integrating equation (3):

$$C = C_0 \exp(-k\frac{m}{V_0}t)(4)$$

By plotting $\ln(\frac{C}{C_0})$ as a function of time t, the constant reaction rate k, can be determined.

In order to validate the theoretical model, aliquots of 1 mL of PNP solution are sampled with a syringe after 30 min of degradation. The solution is placed in a PMMA cuvette to which 1 drop of 3 M HCl solution is added to promote the acidic form of PNP. Measurements are recorded using a UV-VIS spectrophotometer (Genesys 150 UV-VIS from Thermo Scientific) at a wavelength of 317 nm.

2.3.2 Scavenger experiment

Ammonium oxalate and isopropanol are used as, respectively, hole and hydroxyl scavenger at a concentration of 0.05 mM in 50 mL of *p*-nitrophenol aqueous solution filled with ZnO to reach a 1 g/L concentration. Measurements are performed after 30 minutes using a UV-VIS spectrophotometer at a wavelength of 317 nm.

3 Results and discussion

3.1 Composition, morphology, and texture of the ZnO nanoparticles samples

For the three samples, XRD patterns (Figure 1) show the characteristic peaks of the zinc oxide in the wurtzite structure with the three main peaks located between 2 θ = 30° to 40°. The diffractogram corresponding to ZnO A shows peaks with a higher full width at half maximum height (FWHM) than the other two catalysts, meaning a smaller crystallite size, estimated by Scherrer's formula at 5 nm compared to 15 nm for ZnO B and 60 nm for ZnO C (Table 1).

The three main peaks present different intensities between the samples. The higher intensity of the peaks for ZnO C can be explained by the thermal treatment at 550°C, which increases the crystallinity and the crystallite size of the powder.

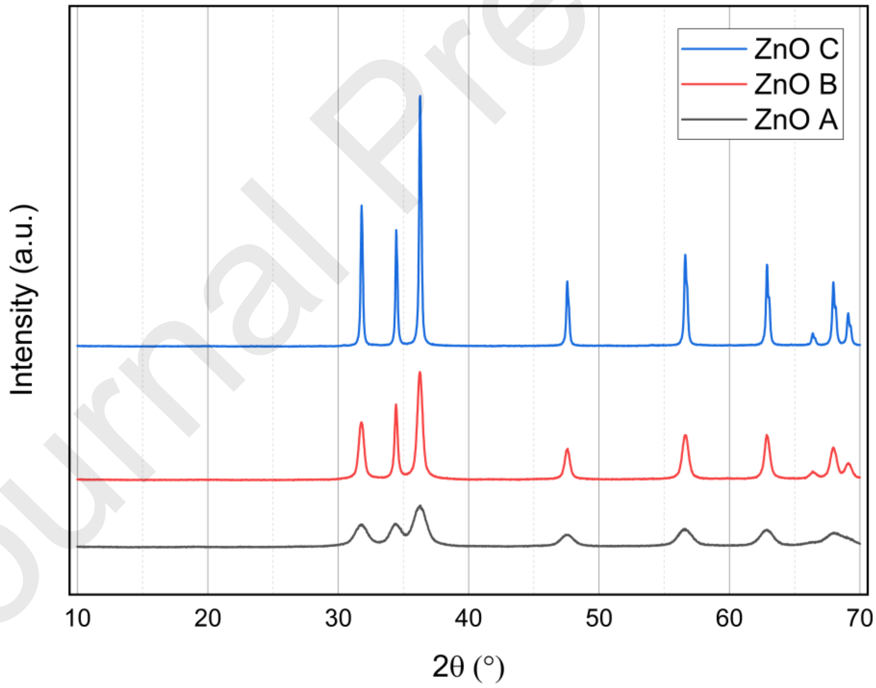

Figure 1. X-ray diffraction patterns for the three powders: ZnO A (black), ZnO B (red), and ZnO C (blue).

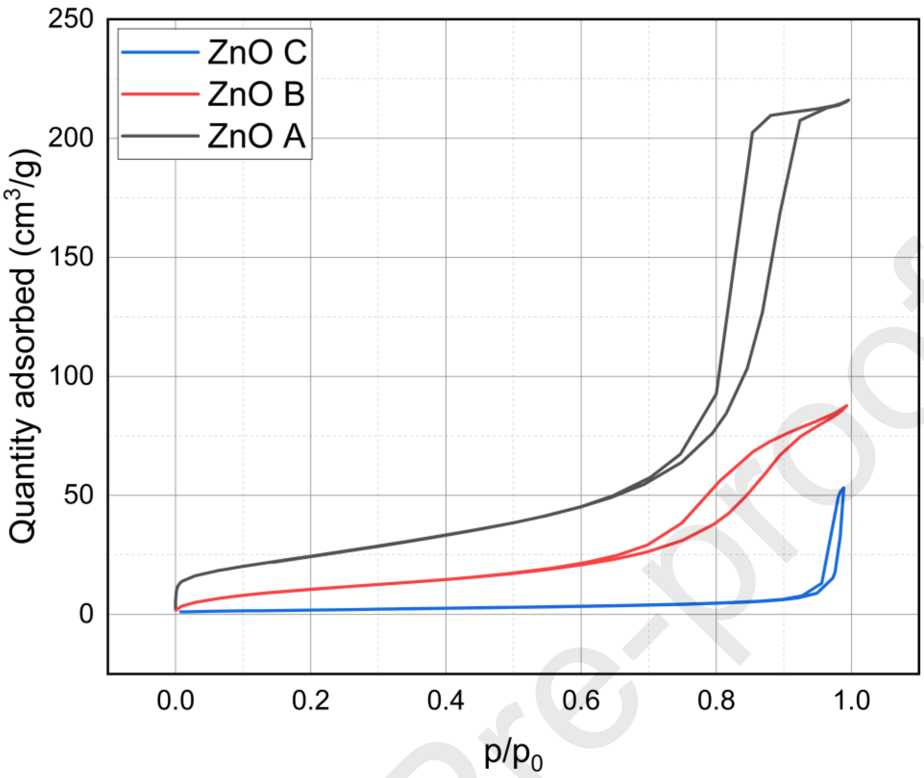

Figure 2. Nitrogen adsorption-desorption isotherms for the three samples, from top to bottom: ZnO A (black), ZnO B (red), ZnO C (blue).

The results obtained by nitrogen adsorption are as follows: ZnO A possesses the highest specific surface area at 90 m^2/g followed by ZnO B at 42 m^2/g, and finally ZnO C at 6 m^2/g. Isotherms (Figure 2) show different shapes: ZnO A (type I + IV) highlights the presence of micro and mesopores within particle aggregates; ZnO B (type I + IV) is made up of micropores and mesopores between the particles also forming aggregates. Finally, for ZnO C (type II), the shape of the isotherm suggests the presence of macropores only between the particles.

These results are in excellent agreement with the crystallite sizes determined by XRD.

Table 1. All data from characterization techniques for the three ZnO samples.

Sample	S_{BET} (m^2/g)	Zeta pot. (mV)	D_{XRD} (nm)	D_{DLS} (nm)	D_{TEM} (nm)	$E_{g,direct}$ (eV)	XPS : Zn & O & C (mol%)	PL_Peak area 1 (PA1)	PL_Peak area 2 (PA2)	PL_Peak area 3 (PA3)	PL_(PA2,3/(PA_1))	k (h^{-1})	k_p ($h^{-1}nm^{-2}$)
ZnO A	90	16	5	552	6	3.29	43; 47; 9	11753	$1.66*10^7$	-	1412	0.74	$9.4*10^{-3}$
ZnO B	42	27	15	120	16	3.32	49; 42; 9	449474	3671503	472205	9	1.87	$2.6*10^{-3}$
ZnO C	6	21	60	490	65	3.33	52; 40; 8	13921	2016865	-	144	0.54	$4*10^{-5}$

S_{BET} = specific surface area; zeta pot. = indication of colloidal stability of the suspension; D_{XRD} = crystallite size calculated thanks to the Scherrer formula from X-ray diffraction (XRD) data; D_{DLS} = hydrodynamic diameter; D_{TEM} = diameter of particle determined by transmission electron microscopy (TEM); $E_{g,direct}$ = direct bandgap; XPS Zn, O, C = mol% of Zn, O, and C calculated from X-ray photoelectron spectroscopy (XPS) data; PL_Peak 1,2, or 3 = photoluminescence area under peak 1, 2, or 3; k = kinetic constant; k_p = kinetic constant based on an isolated particle and equal to $k/(4\pi(D_{XRD}/2))^2$.

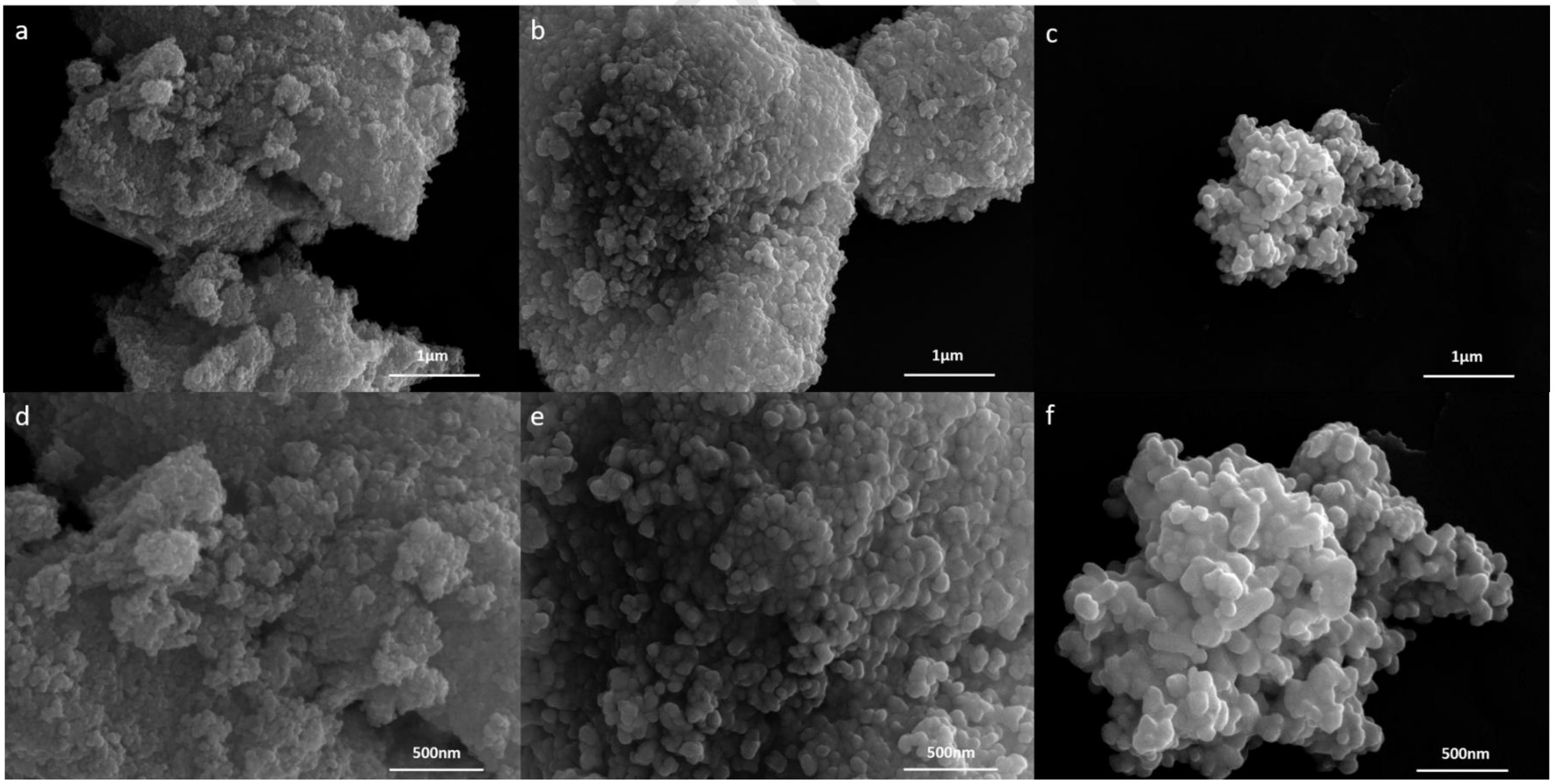

Figure 3. Scanning electron microscope (SEM) images for the three different catalysts at a magnification of 50000× and 100000×: (a, d) ZnO A; (b, e) ZnO B; (c, f) ZnO C.

SEM images (Figure 3) show the morphologies of the three catalysts: they are composed of spheres that aggregate to form larger structures. As can be seen from the TEM images (Figures 4a and 4d), ZnO A exhibits the smallest spheres of 6 nm diameter but the strong aggregation of these small spheres forms large aggregates. For ZnO B (Figure 4b), a very good dispersion is obtained with mainly spheres of 16 nm. Finally, the ZnO C (Figures 4c and 4f), due to the thermal treatment at 550°C, shows particles of 65 nm diameter, which is consistent with results obtained by XRD (Figure 1). The three top images (at lower magnification) of Figure 4 show that aggregates obtained are smaller for ZnO C than those of ZnO A.

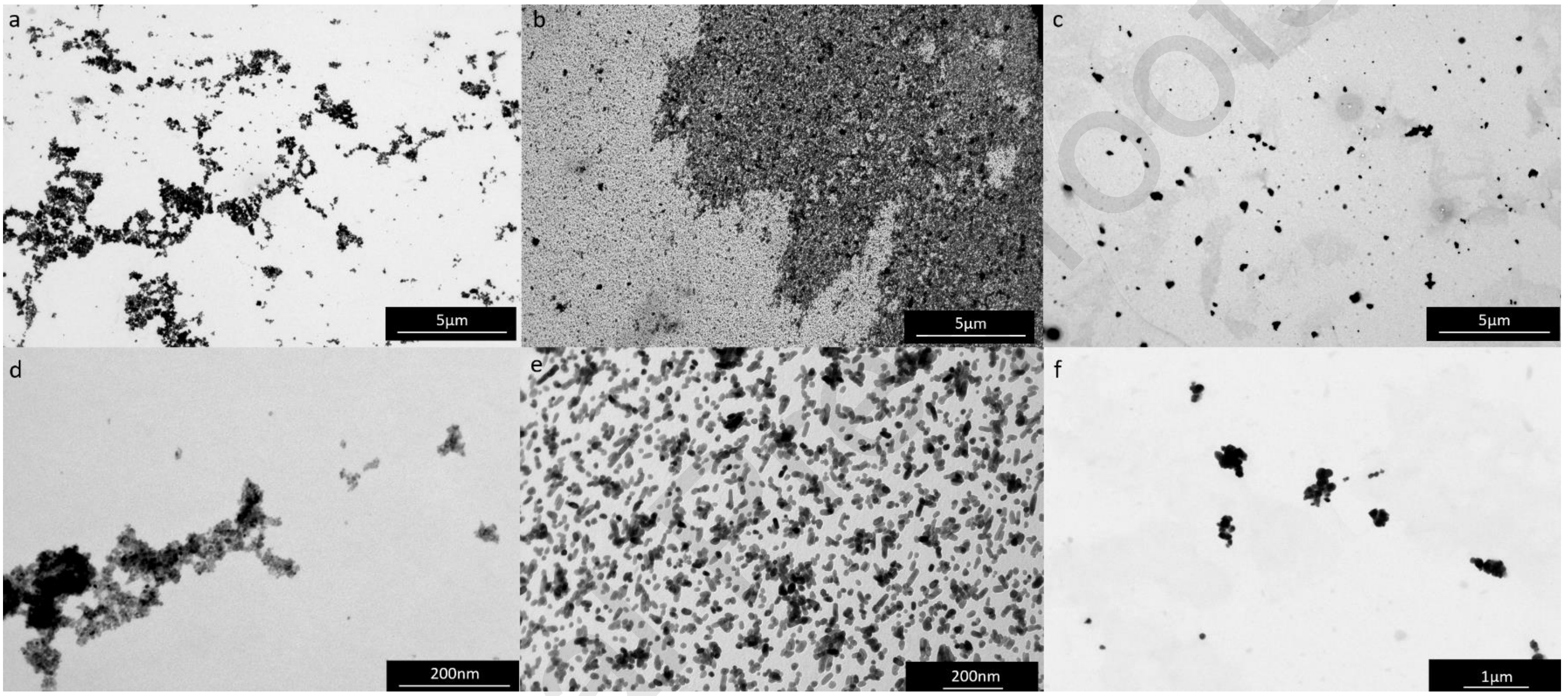

Figure 4. Transmission electron microscope (TEM) images for (a & d) ZnO A, (b & e) ZnO B, and (c & f) ZnO C.

3.2 Optical properties and XPS surface composition

The following paragraphs are devoted to the study of the defects of the three catalysts using photoluminescence and XPS. The formation mechanisms of the different catalysts will also be discussed.

The PL spectra (Figure 5) for the three ZnO catalysts are recorded upon 325 nm excitation in order to cross the band gap of the catalysts. The peak around 380 nm (named peak 1) corresponds to exciton recombination [15] and the other peaks, in the visible (named peak 2) and near IR range (named peak 3), are attributed to the defects present in the crystal lattice [16–18]. By comparing ZnO A with C, the two graphs (Figures 5a and 5c) show some dissimilarities: the maximum of the peak located between 600 nm and 700 nm is slightly shifted towards longer wavelengths for ZnO C (680 nm, compared to 610 nm for ZnO A and B) and a shoulder of the peak is observed at around 600 nm, which suggests that the type of defect differs between the two catalysts. This makes sense as the ZnO C catalyst undergoes a heat treatment at 550°C under static air for 2 h (which also could reduce defects), unlike ZnO A and B which only undergo drying at 100°C [15] [17] [19]

Since photocatalytic activity is affected by the concentration and type of defects, these defects play a crucial role. This concentration passes through an optimum: if the concentration of defects is too high, they act as recombination centers for electrons and holes, whereas if the concentration is optimum, they maximize the lifetime of these electron/hole pairs [20]

By comparing the ratio of the area between exciton peak and defect peak [18], it is possible to classify catalysts from those in which more recombination of electron/hole pairs takes place to those in which there are fewer (or from less defective to more defective: ZnO B < ZnO C < ZnO A) (Table 1). Contrary to what is expected, the more crystalline sample (ZnO C) does not show the lowest amount of defects, which is instead seen in ZnO B. Moreover, the size of agglomerates in ZnO C probably decrease the electron/hole pairs lifetime, which is not the case for the well-dispersed ZnO B. Finally, even if ZnO A shows the largest aggregate size, number of defects could compensate for the negative effect on the electron/hole pairs lifetime [21].

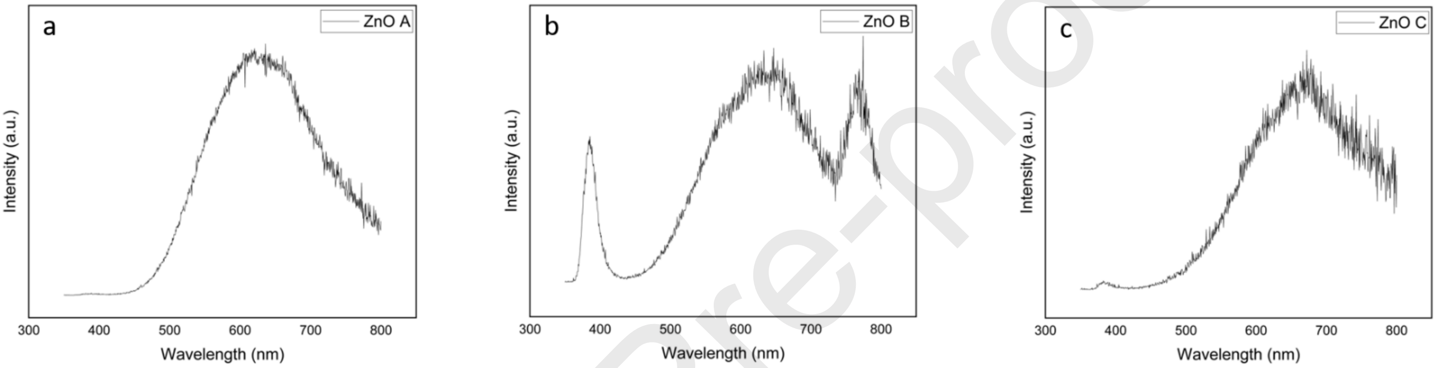

Figure 5. Photoluminescence (PL) spectra (λ_{exc} = 325 nm) for the three ZnO samples: (a) ZnO A, (b) ZnO B, and (c) ZnO C.

XPS data, in Table 1, show the percentage of Zn, O, and C in each catalyst. Considering the O/Zn ratio for the three catalysts (1.1 for ZnO A and 0.8 for ZnO B and C) and subtracting the amount of oxygen coming from carbon contamination (the amount of carbon being almost similar for the three catalysts), the ratio of 0.8 for ZnO B and C implies the presence of metallic zinc. It is possible that the metallic zinc comes from the partial reduction of zinc from ZnO during the XPS analysis.

As the XPS penetration depth is between 5 to 10 nm for ZnO A, with a crystallite and (isolated) particle size of 5 nm, XPS analysis not only involves the surface analysis of the particle but the entire particle, unlike the other two catalysts with larger particle sizes. As the O/Zn ratio is higher (1.1, whereas it should be 1 for perfect ZnO), a conclusion may be that zinc hydroxide ($Zn(OH)_2$) could be present on the surface of the particle. Moreover, the larger amount of $Zn(OH)_2$ present on the particle surface could protect the ZnO from partial reduction to metallic zinc, which is why this ratio remains higher than for the other two catalysts. Looking at the O1s curves in Figure 6a, ZnO A has a larger peak than ZnO B and ZnO C, suggesting the presence of oxygen in another binding state. Oxygen bound to zinc in ZnO bonds has a binding energy of 530 eV, and the shoulder of the ZnO peak towards higher binding energies suggests the presence of zinc hydroxide on the particle surface. However, as reported in the literature [22] this oxygen binding energy could also correspond to oxygen vacancies. It is therefore difficult to distinguish between oxygen from Zn-OH and oxygen vacancies; the latter would be in good agreement with the photoluminescence data. The peak located around 1021 eV on

Figure 6b corresponds to the Zn $2p_{3/2}$, which is characteristic of the zinc binding energy in ZnO [23]. Despite the peaks linked to the oxygen binding energy, no real difference can be observed between them.

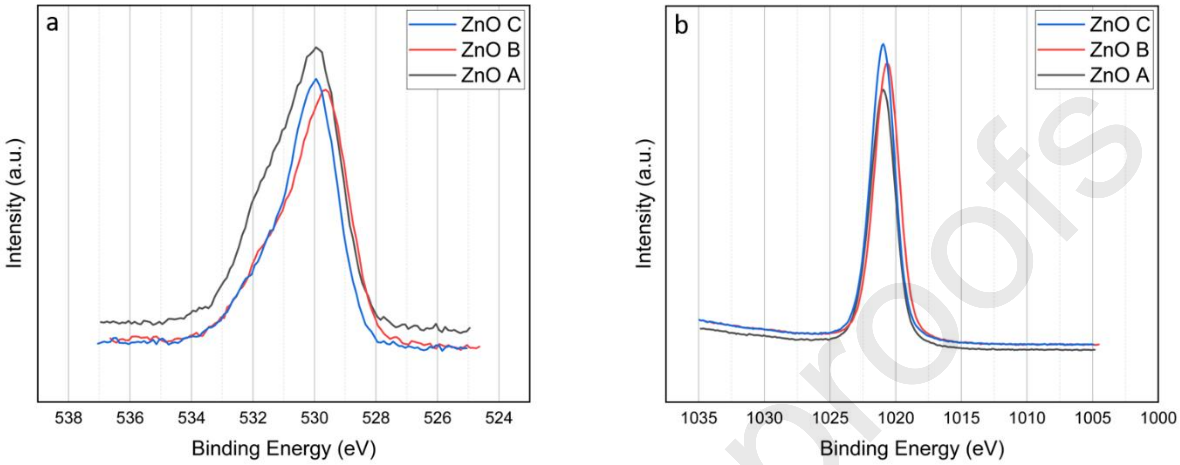

Figure 6. (a) O1s and (b) Zn2p spectra for the three catalysts ZnO A (black), ZnO B (red), and ZnO C (blue)

Finally, the bandgap of the three catalysts was calculated using the Kubelka-Munk function. The three values obtained are fairly close, which is logical given the nature of the catalysts used (pure ZnO [24]): 3.29 eV for ZnO A, 3.32 eV for ZnO B, and 3.3 eV for ZnO C.

3.3 Mechanism of ZnO formation for the three different synthesis routes

3.3.2 ZnO A

The reaction to form ZnO A involves first dissolving the precursors in ethanol at 60 °C as described by equation (5).

$$Zn(Ac)_2.2H_2O \rightarrow Zn^{2+} + 2Ac^{-} + H_2O \quad (5)$$

The addition of potassium hydroxide (as described in section 2.1.2) to the zinc acetate solution increases the pH and shifts the equilibrium towards the formation of $Zn(OH)_2$, which constitutes the nucleation center of zinc oxide [25]. The absence of a surfactant and the viscosity of the solvent play an important role in the particle agglomeration phenomenon [26]. When KOH is added to the zinc acetate solution, $Zn(OH)_2$ forms and precipitates, forming aggregates of different sizes. Crystal synthesis can be summed up in three main stages [27]: (i) atoms attaching to pre-existing crystals, (ii) Ostwald recrystallization, (iii) coalescence.

The viscosity of the solvent plays an important role in the coalescence phenomenon [27]. It decreases at 60°C, increasing the mobility of the species in solution according to equation (6) so that the energy of Brownian motion is greater than the Van Der Waals forces, leading to agglomeration of the particles [27]:

$$\mu = \frac{q}{6\pi\eta r} \quad (6)$$

where μ is the ionic mobility, q is the ionic charge, η is the solvent viscosity, and r is the ion radius.

3.3.3 ZnO B

$$Zn(Ac)_2.2H_2O + DEG \rightarrow ZnO \quad (7)$$

Here the zinc acetate is dissolved in the DEG at 140°C and the water contained in the precursor is necessary for the reaction to occur. The solvent used in this synthesis has different properties compared to ethanol: it is much more viscous (35.7 cP at 20°C) than ethanol (0.57 cP at 60°C). However, the viscosity of the solvent strongly decreases with temperature.

Another parameter seems to have an influence on the dispersion of particles in solution. The solvent acts as a stabilizing agent between the particles, caused by maintaining higher electrostatic forces between the particles and, thus, a better dispersion.

Also, the addition of water destabilizes the colloid by modifying the hydrolysis kinetics of the precursors and reduces the repulsive forces between the particles, leading to precipitation of the ZnO. This explains why only the water contained in the zinc salt precursor is sufficient for the hydrolysis to happen.

3.3.3 ZnO C

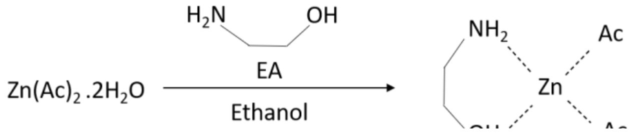

(8)

For the last catalyst, ethanolamine (EA) acts as a stabilizer, dissolving the precursors in solution to form a complex [28] as described by equation (8). This occurs despite the heat treatment used to synthesize zinc oxide (550°C, 2 h), suggesting that particle agglomeration could be limited by the complex formed.

3.4 Photocatalytic degradation of PNP under UV-A

In a typical photocatalyst process, the incident UV-A light promotes electrons from the valence band to the conduction band of ZnO particles, creating electron/hole pairs. These electrons are involved in redox reactions, creating the reactive oxygen species such as hydroxyl groups (OH●) and superoxide anions (O_2●−) [29].

These photo-generated radicals can react with organic pollutants leading to their degradation. In this study. The kinetic model of PNP degradation is assessed in the next paragraphs.

First, the fitted curve of $\ln(\frac{C}{C_0})$ versus time being a straight line (Figure 7), the kinetics are of first order reaction for each catalyst and the kinetic constants can be calculated for each ZnO and are denoted, k, in Table 1. Their evolutions are as follows: ZnO B > ZnO A > ZnO C with a rate constant of 1.87 h^{-1}, 0.74 h^{-1}, and 0.54 h^{-1} for ZnO B, A, and C, respectively (Table 1).

Figure 7

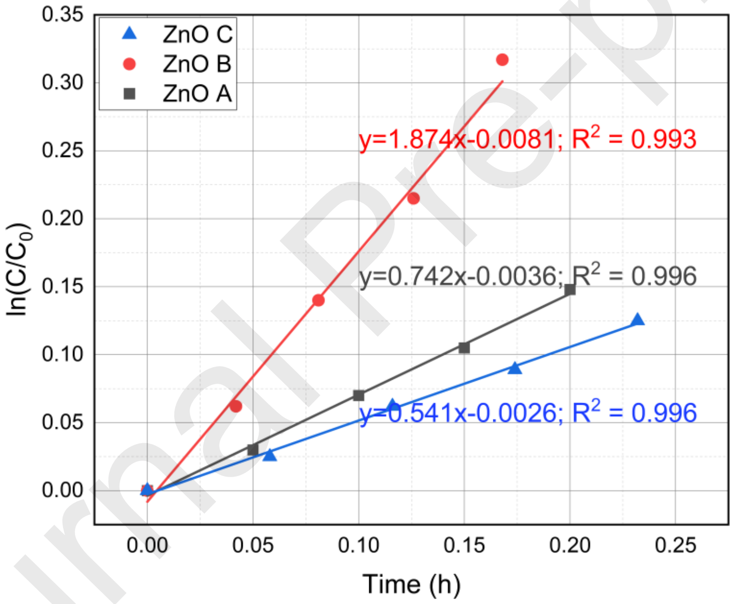

Experimental determination of kinetic constant k of catalyst-mediated degradation by sampling 1 mL of *p*-nitrophenol (PNP) solution at 4 different times. In grey, ZnO A; red, ZnO B; blue, ZnO C

To verify the theoretical values obtained based on the mathematical model developed in section 2.3.1, 1 mL of *p*-nitrophenol solution is collected after illumination under UV-A for 30, 60, and 90 minutes for each catalyst. Figure 8 shows the curve constructed based on equation (4), from experimentally determined k values and considering different times for the PNP degradation. Experimental points are represented in red and show the consistency between the theoretical model and the experimental value.

Scavenger experiments (Figure 9) are carried out to more deeply understand the mechanism behind the PNP degradation by identifying the role of the different radicals produced in the degradation of PNP. The addition of ammonium oxalate (AO) as a hole scavenger prevents water from interacting with the holes formed during illumination, resulting in a drastic reduction in the formation of hydroxyl radicals. Figure 9 shows that, in the presence of AO, the kinetic rates are reduced by a factor of 6 for ZnO A, 9 for ZnO B, and 5 for ZnO C. The trend is similar when isopropanol (IPA) is used as a hydroxyl radical scavenger, with a slight increase in degradation kinetics showing that the action of all the hydroxyls is not inhibited. This is consistent with the results obtained with AO, which inhibits the upstream production of hydroxyl radicals by interacting with the holes formed.

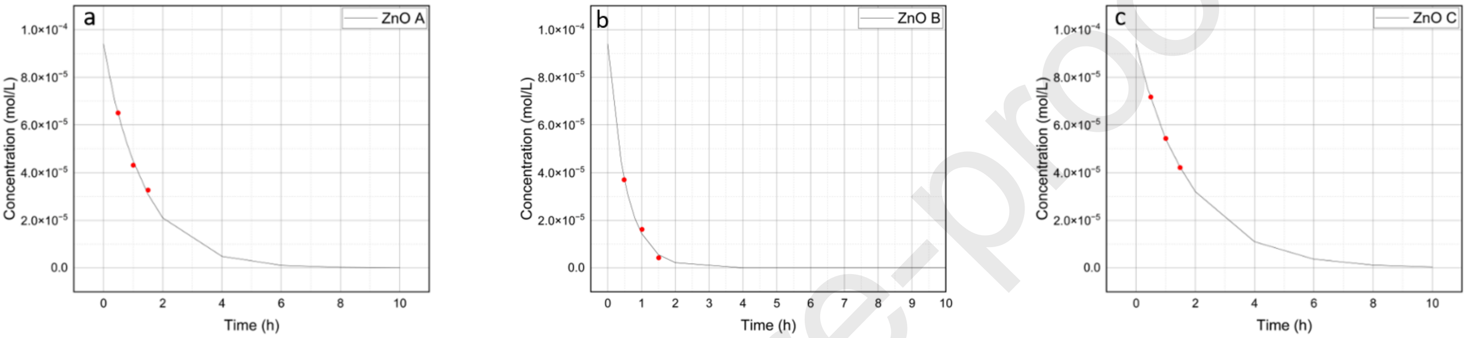

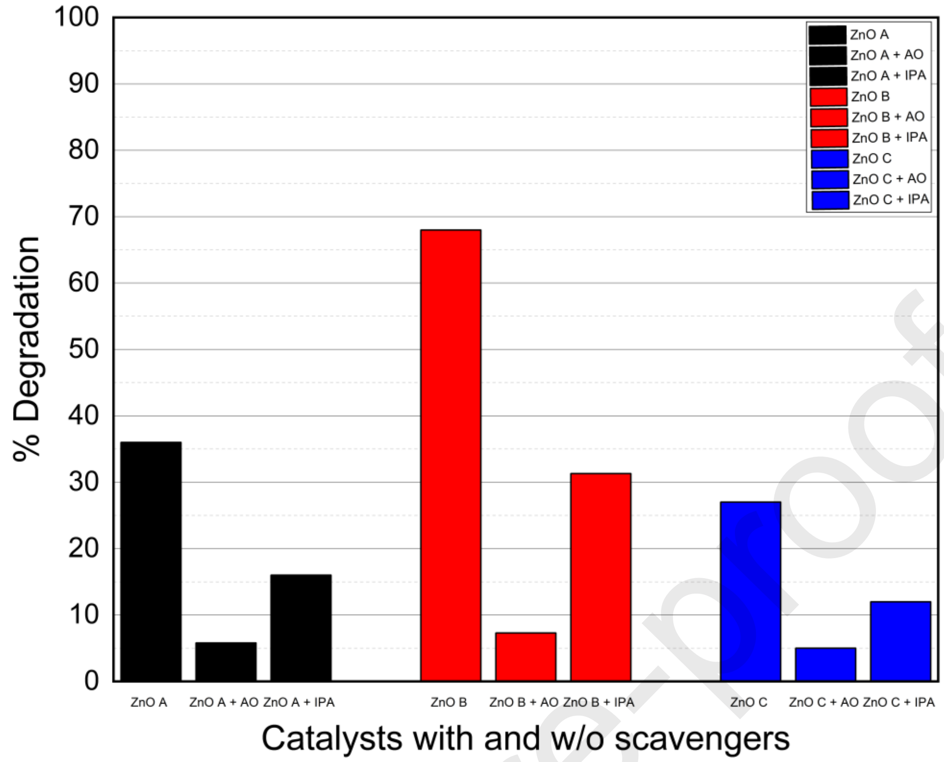

Figure 9. Degradation of *p*-nitrophenol (PNP) by the three catalysts (ZnO A, B, and C) with and without scavenger during 30 min under UV-A illumination. AO = ammonium oxalate, IPA = isopropanol

EPR experiments (Figure 10) can also provide information on hydroxyl radical production kinetics and corroborate data from the scavenger experiment. Using a spin trap such as 5,5-dimethyl-1-pyrroline-N-oxide (DMPO) allows reaction with hydroxyl or superoxide radicals to form an adduct, DMPO-OH and DMPO-OOH, respectively. As the lifetime of the DMPO-OOH adduct is very short [30], only DMPO-OH is detected in the experiments. Spectra shown in Figure 10 confirm that the kinetics of hydroxyl radical production follows the same trend as for the scavenger experiment, with a stronger signal obtained for photocatalyst B than for A and C.

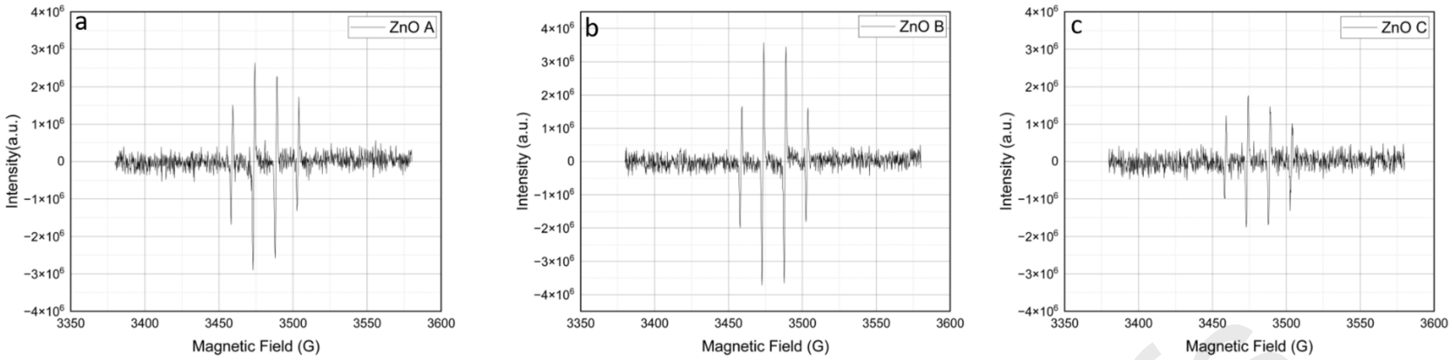

Figure 10. Electron paramagnetic resonance (EPR) spectra for the three catalysts (ZnO A, B, and C) with 5,5-dimethyl-1-pyrroline-N-oxide (DMPO). Spectra are recorded after UV-A illumination for 150 s with DMPO and catalysts at a concentration of 1 g/L.

The following reaction is proposed by other authors [31] for the degradation of PNP by the hydroxyl radical: the C-NO_2 polarity bond, caused by the electron-withdrawing nature of the nitro group and the depletion of the carbon electron, allows the hydroxyl radical to attack this carbon, producing hydroquinone, which decomposes into benzoquinone, which the authors confirmed by GC-MS [31–33]. Next, ring opening producing different species leads to mineralization of the compound.

3.4.1 Surface kinetics of an isolated catalyst particle and discussion on the real case

To identify the key parameters involved in the performance of photocatalysts, the reaction kinetics are considered per surface of an isolated particle (k_p, Table 1), for which the size is obtained by XRD and TEM. The catalyst with the smallest particle size should have the highest degradation rate, but – by considering the present case where the dispersion is not perfect – this is not the case. Looking at the TEM images (Figure 4), the differences in dispersion between the three catalysts are significant. ZnO B shows a large dispersion whereas ZnO A forms large aggregates, leading to greatly reduced catalytic activity. Aggregates do not leave catalytic active sites available for radical production. The mechanism of aggregate formation is discussed in section 3.1. In addition, shadow effects are present when large aggregates are observed [34]. The larger the aggregates, the less the surface opposite the light source is illuminated and the fewer electron/hole pairs are generated, thus reducing the efficiency of the catalyst. In addition, the hydrodynamic diameter obtained by DLS and the zeta potential show notable differences between the photocatalysts since ZnO A has a value of 552 nm and 16 mV, 120 nm and 27 mV for ZnO B, and finally 490 nm and 21 mV for ZnO C, as shown in Table 1. The good dispersion resulting in a lower hydrodynamic radius, a higher zeta potential, and greater colloidal stability underlie the reason why ZnO B has the highest degradation kinetics.

As kinetics are reduced to the surface of a particle, the amount of defects can be related to the degradation kinetic. ZnO A, whose defect peak from photoluminescence spectra (Figure 5a) corresponds to 610 nm, shows the highest kinetics, underlining the importance of defects for photocatalysis performance. ZnO B is a close second, with far fewer defects, but its main defect peak still corresponds to 610 nm, suggesting the same type of defect as ZnO A. However, when looking at ZnO C, which has more defects than ZnO B, the degradation kinetics are slower, and the photoluminescence spectrum (Figure 5c) shows a shift of the defect peak towards longer wavelengths (680 nm), suggesting that this type of defect reduces photocatalyst performance.

In the real case, despite this poorer colloidal stability, the large specific surface area and the amount of defects for the photocatalyst ZnO A are higher than ZnO C, explaining why A's kinetics are slightly better. But, overall, even if ZnO B has a smaller amount of defects, it shows that catalyst dispersion plays a crucial role in the photocatalytic process.

4. Conclusion

In this study, three zinc oxide photocatalysts with different spherical particle sizes were synthesized to determine the degradation kinetics of a typical pollutant, *p*-nitrophenol, under UV-A light. A theoretical model was developed to calculate the rate constant of the degradation reactions, and this was confirmed by experimental data. ZnO B has the highest rate constant k of 1.87 h^{-1} versus 0.74 h^{-1} for ZnO A and 0.54 h^{-1} for ZnO C. Reducing the kinetics to the surface of an isolated particle, which was determined by integrating data from XRD and TEM characterization, the largest degradation kinetics should have been that of ZnO A. However, it was highlighted by TEM and DLS results that the different synthesis routes lead to aggregates of different sizes, leading to less accessibility of the photocatalytic active sites and shadowing effects, thus reducing the efficiency of the photocatalysts. Also, as was shown by photoluminescence and XPS, the type and amount of defects play an important role in photocatalytic performance. ZnO A and B show a defect peak located at 620 nm whereas ZnO C shows a defect peak at 680 nm, suggesting a different type of defect on the surface of the catalyst that reduces the photocatalytic performance. Finally, by considering the real kinetic case (not reduced to the surface of a particle), ZnO B displays the best dispersion with a lower hydrodynamic ratio, resulting in more active sites available for photoreactions and therefore higher PNP degradation.

In addition, a study of the type of radicals involved in *p*-nitrophenol degradation was carried out using scavengers and electron paramagnetic resonance. The use of ammonium oxalate showed a high degree of inhibition of PNP degradation due to its interaction with the holes formed when the photocatalyst is illuminated, preventing the production of hydroxyl radicals, which are therefore the species mainly involved in the degradation of the pollutant. Thanks to the use of DMPO, EPR spectroscopy showed that radical production kinetics are the highest for ZnO B.

Finally, the determining factor is, above all, the size of the particles formed – specifically the size of the aggregates in solution. To maximize pollutant degradation kinetics, the size of the aggregates formed during photocatalyst synthesis must be minimized.

Acknowledgments

Julien G. Mahy, Nathalie Body, Sophie Hermans, and Stéphanie D. Lambert thank the F.R.S.-FNRS for their Postdoctoral Researcher position, FRIA doctoral grant, and Research Directors positions, respectively. J.G.M. is also grateful to the Rotary for a District 2160 grant, to the University of Liège and the FNRS for financial support for a postdoctoral stay in INRS Centre Eau Terre Environnement in Québec, Canada. The authors would like to thank the CARPOR platform of the University of Liège as well as its manager Dr. A. Léonard for the assistance in gas adsorption measurements.

Data availability statement

The raw/processed data required to reproduce these findings cannot be shared at this time as it is part of an ongoing study.

Conflict of interest

The authors declare that there are no conflicts of interest concerning this work.

Ethical approval

The authors declare that they have no known competing financial interests or personal relationships that could have influenced the work reported in this paper.

Consent to participate

All authors agreed to participate to this work.

Consent to publish

All authors agreed to this version for publication.

Authors' contributions

Antoine Farcy: conceptualization, methodology, investigation, formal analysis, writing – original draft, writing – review & editing. Julien G. Mahy: conceptualization, methodology, writing – review & editing, funding acquisition, and project administration. Christelle Alié: investigation, formal analysis, writing – review & editing. Joachim Caucheteux: investigation, formal analysis, writing – review & editing. Dirk Poelman: investigation, formal analysis, writing – review & editing. Zetian Yang: investigation, formal analysis, writing – review & editing. Nathalie Body: investigation, formal analysis, writing – review & editing. Sophie Hermans: investigation, formal analysis, writing – review & editing. Benoît Heinrichs: methodology, writing – review & editing, funding acquisition. Stéphanie D. Lambert: investigation, formal analysis, methodology, writing – review & editing, supervision, funding acquisition, and project administration.

Funding

For their financial support, the authors are grateful to the Ministère de la Région Wallonne Direction Générale des Technologies, de la Recherche et de l'Energie (DGO6) with funding support from the "31st CORNET Call" for the research project "DAF3D - Development of new antibacterial functionalized textiles and 3-D-printed filters for process water treatment".

5. References

[1] J.P. Gutkoski, E.E. Schneider, C. Michels, How effective is biological activated carbon in removing micropollutants? A comprehensive review, J Environ Manage 349 (2024). https://doi.org/10.1016/j.jenvman.2023.119434.

[2] R. T., A. Heydari, A. Henni, State of the Art Treatment of Produced Water, in: Water Treatment, InTech, 2013. https://doi.org/10.5772/53478.

[3] G. Crini, E. Lichtfouse, Advantages and disadvantages of techniques used for wastewater treatment, Environ Chem Lett 17 (2019) 145–155. https://doi.org/10.1007/s10311-018-0785-9.

[4] Y. Deng, R. Zhao, Advanced Oxidation Processes (AOPs) in Wastewater Treatment, Curr Pollut Rep 1 (2015) 167–176. https://doi.org/10.1007/s40726-015-0015-z.

[5] J.G. Mahy, C. Wolfs, A. Mertes, C. Vreuls, S. Drot, S. Smeets, S. Dircks, A. Boergers, J. Tuerk, S.D. Lambert, Advanced photocatalytic oxidation processes for micropollutant elimination from municipal and industrial water, J Environ Manage 250 (2019). https://doi.org/10.1016/j.jenvman.2019.109561.

[6] A.Z. Fadhel, P. Pollet, C.L. Liotta, C.A. Eckert, Combining the benefits of homogeneous and heterogeneous catalysis with tunable solvents and nearcritical water, Molecules 15 (2010) 8400–8424. https://doi.org/10.3390/molecules15118400.

[7] J. Lai, W. Niu, R. Luque, G. Xu, Solvothermal synthesis of metal nanocrystals and their applications, Nano Today 10 (2015) 240–267. https://doi.org/10.1016/j.nantod.2015.03.001.

[8] Y.X. Gan, A.H. Jayatissa, Z. Yu, X. Chen, M. Li, Hydrothermal Synthesis of Nanomaterials, J Nanomater 2020 (2020). https://doi.org/10.1155/2020/8917013.

[9] A. Kumar, Y. Kuang, Z. Liang, X. Sun, Microwave chemistry, recent advancements, and eco-friendly microwave-assisted synthesis of nanoarchitectures and their applications: a review, Mater Today Nano 11 (2020). https://doi.org/10.1016/j.mtnano.2020.100076.

[10] D. Ward, E.I. Ko, P.D. Metal Alkorides, D.C. Chem, Sol-Gel Science: The Physics and Chemistry of Sol-Gel Processing, Ind. Eng. Chem. Res. 34 (1995) 421–433.

[11] S. Pooyan spooyan, Sol-gel process and its application in Nanotechnology, Journal of Polymer Engineering and Technology 13 (2005) 38–41. http://polymer.aut.ac.ir/.

[12] R. Kumar, G. Kumar, A. Umar, Zinc oxide nanomaterials for photocatalytic degradation of methyl orange: A review, Nanoscience and Nanotechnology Letters 6 (2014) 631–650. https://doi.org/10.1166/nnl.2014.1879.

[13] J.G. Mahy, C.A. Paez, C. Carcel, C. Bied, A.S. Tatton, C. Damblon, B. Heinrichs, M. Wong Chi Man, S.D. Lambert, Porphyrin-based hybrid silica-titania as a visible-light photocatalyst, J Photochem Photobiol A Chem 373 (2019) 66–76. https://doi.org/10.1016/j.jphotochem.2019.01.001.

[14] S.L. Pirard, C.M. Malengreaux, D. Toye, B. Heinrichs, How to correctly determine the kinetics of a photocatalytic degradation reaction?, Chemical Engineering Journal 249 (2014) 1–5. https://doi.org/10.1016/j.cej.2014.03.088.

[15] M.D. McCluskey, S.J. Jokela, Defects in ZnO, J Appl Phys 106 (2009). https://doi.org/10.1063/1.3216464.

[16] Y. Huang, Y. Yu, Y. Yu, B. Zhang, Oxygen Vacancy Engineering in Photocatalysis, Solar RRL 4 (2020). https://doi.org/10.1002/solr.202000037.

[17] M. Wang, Y. Zhou, Y. Zhang, E. Jung Kim, S. Hong Hahn, S. Gie Seong, Near-infrared photoluminescence from ZnO, Appl Phys Lett 100 (2012). https://doi.org/10.1063/1.3692584.

[18] A. Farcy, S.D. Lambert, D. Poelman, Z. Yang, F. Drault, S. Hermans, P. Drogui, B. Heinrichs, C. Malherbe, G. Eppe, A. Verdin, J.G. Mahy, Influence of crystallographic facet orientations of sol-gel ZnO on the photocatalytic degradation of p-nitrophenol in water, J Solgel Sci Technol (2024). https://doi.org/10.1007/s10971-023-06301-9.

[19] N.M. Flores, U. Pal, R. Galeazzi, A. Sandoval, Effects of morphology, surface area, and defect content on the photocatalytic dye degradation performance of ZnO nanostructures, RSC Adv 4 (2014) 41099–41110. https://doi.org/10.1039/c4ra04522j.

[20] J. Fang, H. Fan, Y. Ma, Z. Wang, Q. Chang, Surface defects control for ZnO nanorods synthesized by quenching and their anti-recombination in photocatalysis, Appl Surf Sci 332 (2015) 47–54. https://doi.org/10.1016/j.apsusc.2015.01.139.

[21] A. Falamas, I. Marica, A. Popa, D. Toloman, S. Pruneanu, F. Pogacean, F. Nekvapil, T.D. Silipas, M. Stefan, Size-dependent spectroscopic insight into the steady-state and time-resolved optical properties of ZnO photocatalysts, Mater Sci Semicond Process 145 (2022). https://doi.org/10.1016/j.mssp.2022.106644.

[22] W.-Y. Chen, J.-S. Chen, J.-S. Jeng, Suppression of Oxygen Vacancy and Enhancement in Bias Stress Stability of High-Mobility ZnO Thin-Film Transistors with N 2 O Plasma Treated MgO Gate Dielectrics , ECS Journal of Solid State Science and Technology 2 (2013) P287–P291. https://doi.org/10.1149/2.001307jss.

[23] T. Du, H. Song, O.J. Ilegbusi, Sol-gel derived ZnO/PVP nanocomposite thin film for superoxide radical sensor, Materials Science and Engineering C 27 (2007) 414–420. https://doi.org/10.1016/j.msec.2006.05.040.

[24] R. Rusdi, A.A. Rahman, N.S. Mohamed, N. Kamarudin, N. Kamarulzaman, Preparation and band gap energies of ZnO nanotubes, nanorods and spherical nanostructures, Powder Technol 210 (2011) 18–22. https://doi.org/10.1016/j.powtec.2011.02.005.

[25] M. Wang, Y. Zhou, Y. Zhang, S.H. Hahn, E.J. Kim, From Zn(OH)2 to ZnO: A study on the mechanism of phase transformation, CrystEngComm 13 (2011) 6024–6026. https://doi.org/10.1039/c1ce05502j.

[26] C. Wang, E. Shen, E. Wang, L. Gao, Z. Kang, C. Tian, Y. Lan, C. Zhang, Controllable synthesis of ZnO nanocrystals via a surfactant-assisted alcohol thermal process at a low temperature, Mater Lett 59 (2005) 2867–2871. https://doi.org/10.1016/j.matlet.2005.04.031.

[27] H. Teterycz, O. Rac, P. Suchorska-Woźniak, THE FORMATION MECHANISM OF COLLOIDAL SPHERES OF ZnO IN ETHYLENE GLYCOL, Dig J Nanomater Biostruct 8 (2013) 1157–1167.

[28] A. Gómez-Núnez, S. Alonso-Gil, C. López, P. Roura, A. Vilà, Role of Ethanolamine on the Stability of a Sol-Gel ZnO Ink, Journal of Physical Chemistry C 121 (2017) 23839–23846. https://doi.org/10.1021/acs.jpcc.7b09935.

[29] N. Laouedj, ZnO-Assisted Photocatalytic Degradation of Congo Red and Benzopurpurine 4B in Aqueous Solution, Journal of Chemical Engineering & Process Technology 02 (2011). https://doi.org/10.4172/2157-7048.1000106.

[30] G.R. Buettner, THE SPIN TRAPPING OF SUPEROXIDE AND HYDROXYL FREE RADICALS WITH DMPO (5,5-DIMETHYLPYRROLINE-N-OXIDE): MORE ABOUT IRON, Free Radic Res Commun. 19 (1993) 79–87.

[31] X. Tian, X. Wang, Y. Nie, C. Yang, D.D. Dionysiou, Hydroxyl radical-involving p-nitrophenol oxidation during its reduction by nanoscale sulfidated zerovalent iron under anaerobic conditions, Environ Sci Technol 55 (2021) 2403–2410. https://doi.org/10.1021/acs.est.0c07475.

[32] A. Di Paola, V. Augugliaro, L. Palmisano, G. Pantaleo, E. Savinov, Heterogeneous photocatalytic degradation of nitrophenols, 2003.

[33] N. Kimura, W. Kitagawa, Y. Kamagata, Biodegradation of nitrophenol compounds, Environmental Science and Engineering (Subseries: Environmental Science) 112 (2014). https://doi.org/10.1007/978-3-319-01083-0_1.

[34] J.G. Mahy, F. Deschamps, V. Collard, C. Jérôme, J. Bartlett, S.D. Lambert, B. Heinrichs, Acid acting as redispersing agent to form stable colloids from photoactive crystalline aqueous sol–gel TiO2 powder, J Solgel Sci Technol 87 (2018) 568–583. https://doi.org/10.1007/s10971-018-4751-6.

Authors' contributions

Antoine Farcy: conceptualization, methodology, investigation, formal analysis, writing – original draft, writing – review & editing. Julien G. Mahy: conceptualization, methodology, writing – review & editing, funding acquisition, and project administration. Christelle Alié: investigation, formal analysis, writing – review & editing. Joachim Caucheteux: investigation, formal analysis, writing – review & editing. Dirk Poelman: investigation, formal analysis, writing – review & editing. Zetian Yang: investigation, formal analysis, writing – review & editing. Nathalie Body: investigation, formal analysis, writing – review & editing. Sophie Hermans: investigation, formal analysis, writing – review & editing. Benoît Heinrichs: methodology, writing – review & editing, funding acquisition. Stéphanie D. Lambert: investigation, formal analysis, methodology, writing – review & editing, supervision, funding acquisition, and project administration.

- Three ZnO with similar spherical morphology but different sizes are synthesized by sol-gel methods.

- ZnO A and B show a defect peak located at 620nm while ZnO C is located at 680 nm, suggesting a different type of defect reducing the photocatalytic performances.
- The size of the aggregates induced by the synthesis methods play a more important role in the catalytic activity of the three ZnO samples than defects.
- Kinetics three times higher for the catalyst with the best dispersion.
- The catalyst with the best dispersion produces the highest amount of hydroxyl radicals.